nature physics

LETTERS

https://doi.org/10.1038/s41567-020-1002-x

Check for updates

# Chemotaxis under flow disorder shapes microbial dispersion in porous media

Pietro de Anna[1], Amir A. Pahlavan[2], Yutaka Yawata[3], Roman Stocker[4,5]✉ and Ruben Juanes[5,6]✉

**Natural soils are host to a high density[1] and diversity[2] of microorganisms, and even deep-earth porous rocks provide a habitat for active microbial communities[3]. In these environments, microbial transport by disordered flows is relevant for a broad range of natural and engineered processes, from biochemical cycling to remineralization and bioremediation[4–7]. Yet, how bacteria are transported and distributed in the subsurface as a result of the disordered flow and the associated chemical gradients characteristic of porous media has remained poorly understood, in part because studies have so far focused on steady, macroscale chemical gradients[8–10]. Here, we use a microfluidic model system that captures flow disorder and chemical gradients at the pore scale to quantify the transport and dispersion of the soil-dwelling bacterium *Bacillus subtilis* in porous media. We observe that chemotaxis strongly modulates the persistence of bacteria in low-flow regions of the pore space, resulting in a 100% increase in their dispersion coefficient. This effect stems directly from the strong pore-scale gradients created by flow disorder and demonstrates that the microscale interplay between bacterial behaviour and pore-scale disorder can impact the macroscale dynamics of biota in the subsurface.**

In microbial habitats other than soils, such as the ocean, it has been shown that large-scale dynamics are often driven by the collective action of the behaviour of microorganisms at the level of individuals—in particular, behaviours to sense and exploit resource gradients and enhance resource uptake[11–13]. The spatial distribution of microbial resource gradients is largely shaped by fluid stirring and mixing, which create or enhance heterogeneity or 'patchiness', as demonstrated by turbulence in the ocean[14,15]. An important feature of turbulent flows is the spatio-temporal complexity of fluid velocity, which is responsible for stretching nutrient patches to create strong gradients at the microscale—the so-called Batchelor scale (30–300 μm in the ocean[16]). The ability of motile chemotactic bacteria to cover that scale within the lifespan of the nutrient patch affords them a competitive advantage in turbulent flows[16]. Much less is known about the role of behavioural adaptations in subsurface environments such as soils and rocks, where flow takes places in confined spaces through an intricate maze of pores, which can be occupied by fluids, amidst solid grains. Here, turbulence is absent (typical Reynolds numbers are well below unity), yet strong chemical gradients can exist due to flow disorder as a consequence of the heterogeneous structure of the solid porous matrix[17,18]. This raises the fundamental question of whether motility affords microorganisms a competitive advantage in the subsurface.

The transport of bacteria in porous media is affected by both the structure of the medium and by chemical gradients[8–10,19–22]. Important insights have been gained from sand-packed column experiments and modelling of the impact of microbial swimming and chemotaxis on the macroscopic transport and residence time of bacteria, as evidenced by breakthrough curves of microbial suspensions[23,24]. These studies have indirectly inferred longer retention times of chemotactic bacteria in low-permeability regions[25]. Other studies have examined chemotaxis at the pore scale in a microfluidic device[19], translating chemotactic behaviour into a dispersion coefficient[26], but under steady homogeneous gradients. Thus, studies so far have focused on either macroscale observables of bacterial displacements in porous media or pore-scale studies under steady, transverse chemical gradients. It is now known, however, that strong spatio-temporal flow heterogeneity occurs at the pore scale. Direct observations and modelling have recently provided new insights into the physico-chemical environment that characterizes the subsurface at the pore scale—the scale at which microorganisms interact with the surrounding fluid. This environment is characterized by strong spatial flow disorder[27,28], intermittent Lagrangian velocities[29,30] and large microscale gradients[17,18]. Recognizing these recent insights, here we study how the physico-chemical dynamics at the pore scale affect microbial dispersion, using spatially and temporally resolved observations in a microfluidics model system through time-lapse video microscopy.

We used a microfluidics device[31,32] as an analogue for a porous medium and took advantage of the flexibility afforded by micro-fabrication based on soft lithography to recreate the geometrical complexity mimicking a simplified subsurface environment. We fabricated a microchannel (45 mm × 5.2 mm × 0.1 mm) containing a random distribution of cylindrical obstacles with either circular or crescent-shaped cross-section, with the distance between pore walls ('pore openings') ranging between 0.05 and 0.7 mm (Fig. 1a,b). The channel depth, $a = 0.1$ mm, is comparable to the average pore opening, $\lambda = 0.2$ mm (representative of many common geological structures, such as karst formations or soils[33]). This range of values of $a/\lambda$ of order 1 yields parabolic-like velocity profiles in both vertical and horizontal directions between posts, and results in a heterogeneous velocity distribution at the mid-depth, horizontal observation plane (Fig. 1c,d), as verified by particle image velocimetry (PIV). The effect of this heterogeneity is the emergence of a strong spatial correlation in the velocity field, in the form of fast

[1]Institute of Earth Sciences, University of Lausanne, Lausanne, Switzerland. [2]Department of Mechanical and Aerospace Engineering, Princeton University, Princeton, NJ, USA. [3]Faculty of Life and Environmental Sciences, University of Tsukuba, Tsukuba, Japan. [4]Institute of Environmental Engineering, Department of Civil, Environmental and Geomatic Engineering, ETH Zurich, Zurich, Switzerland. [5]Department of Civil and Environmental Engineering, Massachusetts Institute of Technology, Cambridge, MA, USA. [6]Department of Earth, Atmospheric and Planetary Sciences, Massachusetts Institute of Technology, Cambridge, MA, USA. ✉e-mail: romanstocker@ethz.ch; juanes@mit.edu

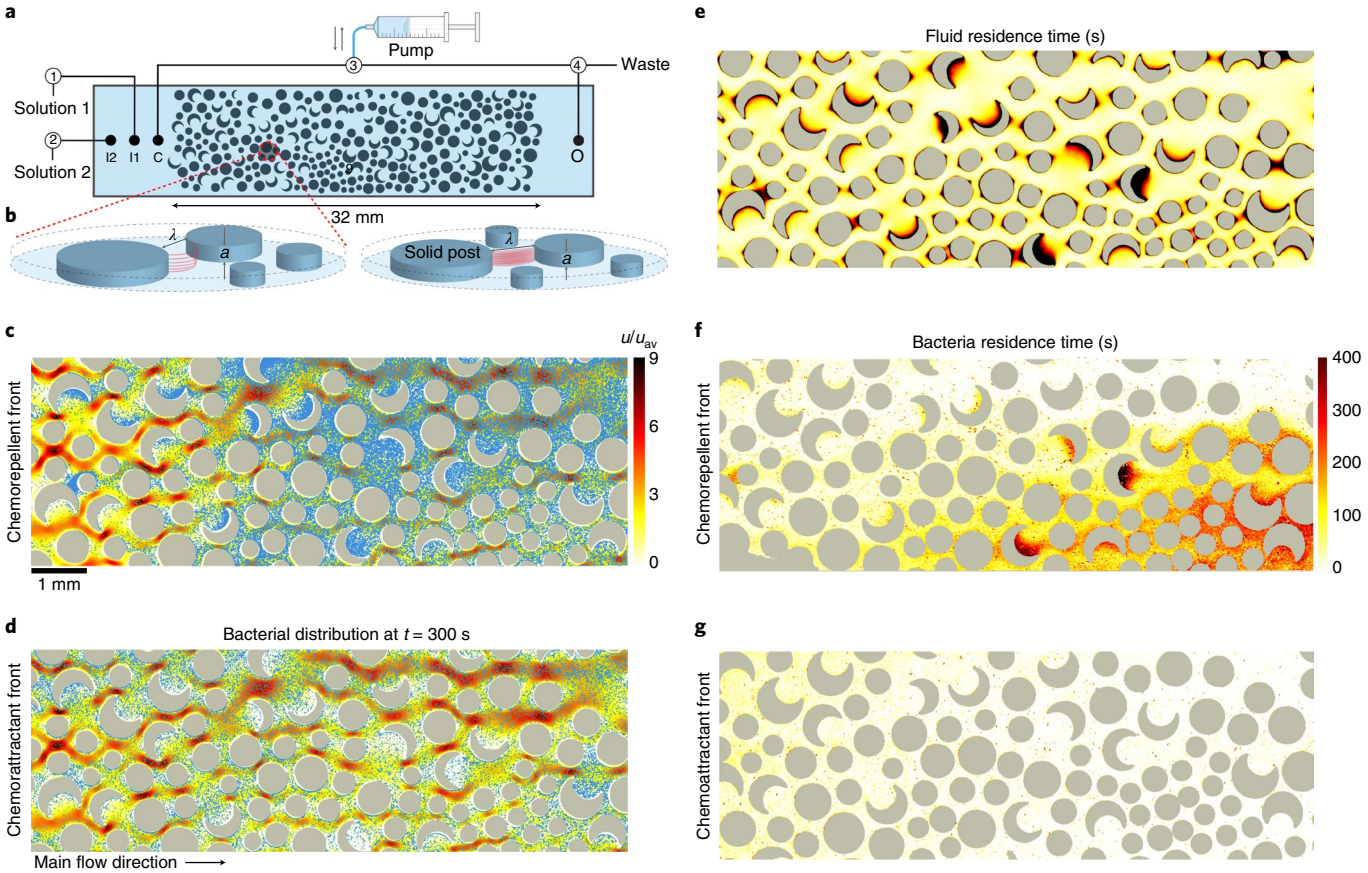


**Fig. 1 | Chemotaxis at the pore scale drives the local residence time of bacteria in porous media. a**, Schematic of the microfluidics set-up. The device consists of a disordered arrangement of disks and crescent-shaped obstacles, serving as an analogue for porous media. A syringe pump withdraws fluid at a constant flow rate $Q = 0.01\,\mu l\,s^{-1}$. Valves (numbered) are used to initially fill the device with a first solution and then create a sharp front of a second solution (Supplementary Section II.C). **b**, Enlargement of a portion of the microfluidics device, showing the definition of the pore width $\lambda$ and channel depth *a*. **c**, Spatial distribution of *Bacillus subtilis* sp. bacteria (blue dots) in response to a chemorepellent injection, superposed on the map of fluid velocity $u$ (rescaled by its average value, $u_{av}$; Supplementary Section IV). As a result of pore disorder, the velocity field exhibits high-velocity channels (dark red) and low-velocity micropockets (light yellow). **d**, As in **c**, but for a chemoattractant injection. The colour bar next to **c** also applies to **d**. **e**, Map of fluid local residence time (in seconds), representing the time required for a small fluid volume to be displaced by 1 pixel (1.1 μm). **f**, Map of bacterial local residence time for a chemorepellent injection, defined for each pixel as the total time over which that pixel contains bacteria, over a 40-min experiment. **g**, As in **f**, but for a chemoattractant injection. The colour bar next to **f** also applies to **e** and **g**.

flow pathways and areas of fluid stagnation (Fig. 1c–e), as observed in both 2D simplified media[29] and real rocks[28]. As a result, transported substances will be deformed through elongation and stretching by the velocity gradients within individual pores[17,28,29].

To study the effect of motility on microbial dispersion within the described porous medium, we imaged, over time, the spatial distribution of a suspended population of *B. subtilis* sp. (strain OI1085), a soil-dwelling bacterium that swims at $8.0 \pm 5.0\,\mu m\,s^{-1}$ in stagnant fluid (Supplementary Section I). We initially filled the microchannel with the 'defending' bacterial suspension, a phosphate-buffered saline (PBS) solution of $5\,mg\,ml^{-1}$ tryptone. We selected a bacterial concentration of $n_0 \approx 10^8$ cells per ml, which is dense enough to allow for accurate imaging (Supplementary Section III) and dilute enough that it should not ostensibly affect tryptone diffusion or tryptone consumption over the timescale of the experiment (Supplementary Section I).

The experiment was initiated by triggering a sharp invading front (Supplementary Section II.C) of a solution containing either a higher ($50\,mg\,ml^{-1}$) or lower ($0\,mg\,ml^{-1}$) tryptone concentration, displacing the defending suspension. Each experiment was replicated four times. The high concentration of tryptone ($50\,mg\,ml^{-1}$) makes the invading solution in the first case a chemoattractant, while zero concentration of tryptone makes the invading solution in the second case a negative-chemoattractant, as confirmed in separate, no-flow experiments (Extended Data Figs. 1 and 2 and Supplementary Section I) using an established microfluidics chemotaxis assay[34]. Throughout this work we refer to this negative-chemoattractant solution as a chemorepellent (in the sense that bacteria will chemotax away from the invading solution; tryptone of course remains a chemoattractant). These chemotaxis experiments also provided a quantification of the chemotactic migration velocity of bacteria, which was found to be $u_c = 0.9 \pm 0.1\,\mu m\,s^{-1}$ for the chemoattractant case and $u_c = 1.6 \pm 0.1\,\mu m\,s^{-1}$ for the chemorepellent case (Extended Data Fig. 2 and Supplementary Section I).

Time-lapse imaging of the distribution of *B. subtilis* sp. (blue dots, Fig. 1b,c, Extended Data Fig. 3 and Supplementary Section III) over 40 min showed that the dispersion rate and residence time of the bacteria depend strongly on their chemotactic behaviour, which in turn is driven by the pore-scale chemical gradients. Bacteria are swept away by the invading fluid front, except in low-flow micropockets, which are regions where the fluid velocity is low (Fig. 1e) and thus chemical flushing is weak. In these micropockets, small

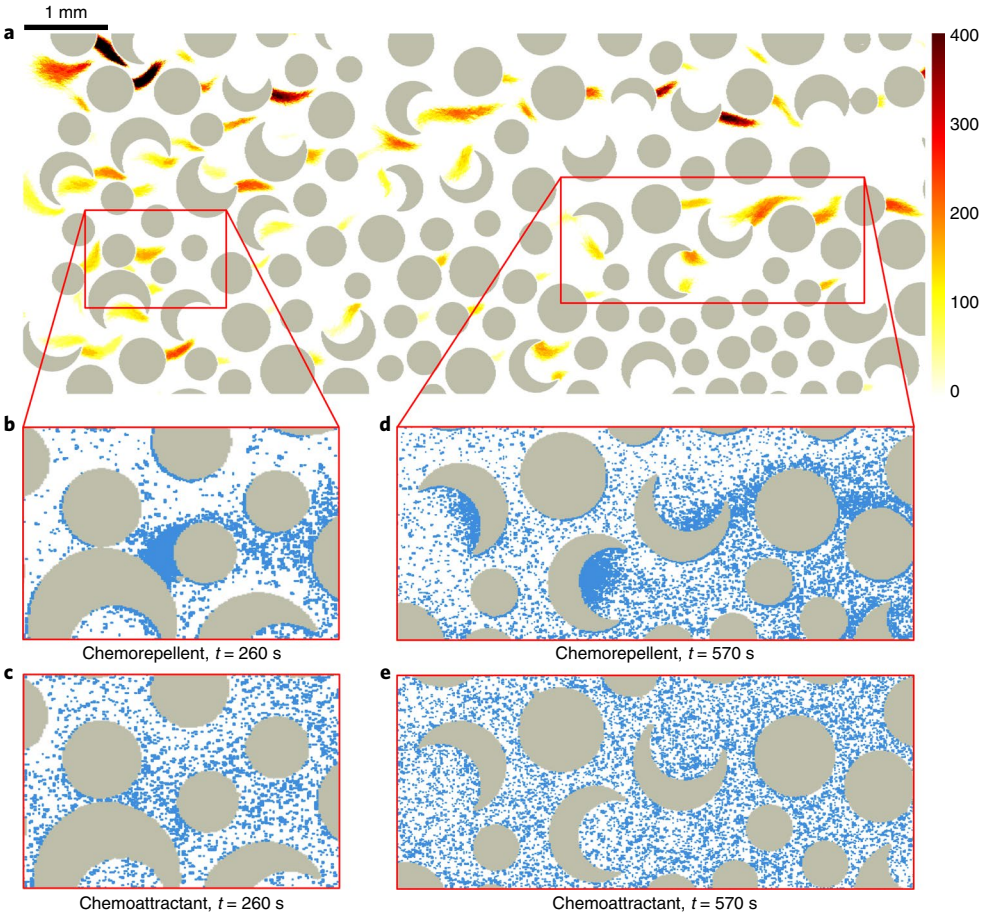


**Fig. 2 | Increased persistence time of bacteria is caused by local accumulation in micropockets. a**, The residence time of the invading chemical gradients (of either chemoattractant or chemorepellent, in seconds), defined as the time for which a given pixel harbours a detectable concentration gradient (Supplementary Section V.B). **b**–**e**, Snapshots of bacterial spatial distribution over two selected areas at two different times during a chemorepellent injection (**b** and **d**) and a chemoattractant injection (**c** and **e**), respectively, evidencing the ability of *B. subtilis* to chemotax towards low-velocity micropockets during chemorepellent injection and out of them during chemoattractant injection. The persistence of chemical gradients provides the mechanism for the sustained chemotaxis over timescales much longer than the characteristic pore-scale diffusion timescale.

volumes of the defending fluid persist, and around them the invading front generates strong and temporally persistent chemical gradients. We isolated the hydrodynamic control on bacterial flushing by using a reference no-gradients experiment, in which we injected an invading front of spent medium (obtained by centrifugation of an aliquot of the bacterial culture) into a defending bacterial suspension. Compared to this reference case, the injection of a chemorepellent solution promotes the accumulation of bacteria in the micropockets, increasing their residence time (Fig. 1f), whereas the injection of a chemoattractant solution elicits migration of bacteria up the chemical gradients and away from low-velocity zones, decreasing their residence time (Fig. 1g). Superposition of the spatial distribution of bacteria and the flow field supports this conclusion (Fig. 1c,d and Supplementary Videos 1–4), where the flow field was imaged in separate PIV experiments in the same microfluidic device in the absence of bacteria (Extended Data Figs. 4 and 5, and Supplementary Section IV).

To further support this observation, we computed the timescale over which chemical gradients persisted against the action of molecular diffusion, and showed that it is sufficient for pore-scale chemotactic migration of the bacteria. The longevity of bacterial accumulation in micropockets after the passage of a chemorepellent front is surprising, if one considers the dilution of the front at the scale of a single pore by diffusion alone. The characteristic time for gradients to dissipate by molecular diffusion in the average pore is $\tau_D = \lambda^2/D_s \approx 60$ s, where $D_s = 7 \times 10^{-4}$ mm$^2$ s$^{-1}$ is the molecular diffusion coefficient of the chemoattractant[35]. Because the bacterial residence time in the micropockets is up to 300 s longer for the chemorepellent front compared to the chemoattractant front (Fig. 1f,g), chemotaxis and thus chemical gradients must persist over a timescale much longer than $\tau_D$.

To demonstrate that the timescale over which chemical gradients are sustained is considerably larger than the molecular diffusion timescale $\tau_D$, we performed an experiment without bacteria in which we added a fluorescent dye of diffusivity $D_s = 6.6 \times 10^{-4}$ mm$^2$ s$^{-1}$, similar to that of tryptone, to the invading solution (Extended Data Figs. 6–8 and Supplementary Section V). By imaging over time, we quantified the spatial gradients in dye concentration and their persistence time. The spatial map of gradient persistence time (Fig. 2a) explains the sustained local accumulation of bacteria by chemotaxis: pockets with high bacterial concentrations (Fig. 2b,d) are bounded by regions in which gradients persist for times on the order of 300 s, and often longer (Fig. 2a). This implies that the chemical gradients driving bacteria into the micropockets must be sustained by a physical mechanism that modulates and slows molecular diffusion.

The physical mechanism that maintains chemical gradients in micropockets is enhanced longitudinal dispersion of the solute front due to shear and flow disorder. To test this hypothesis,

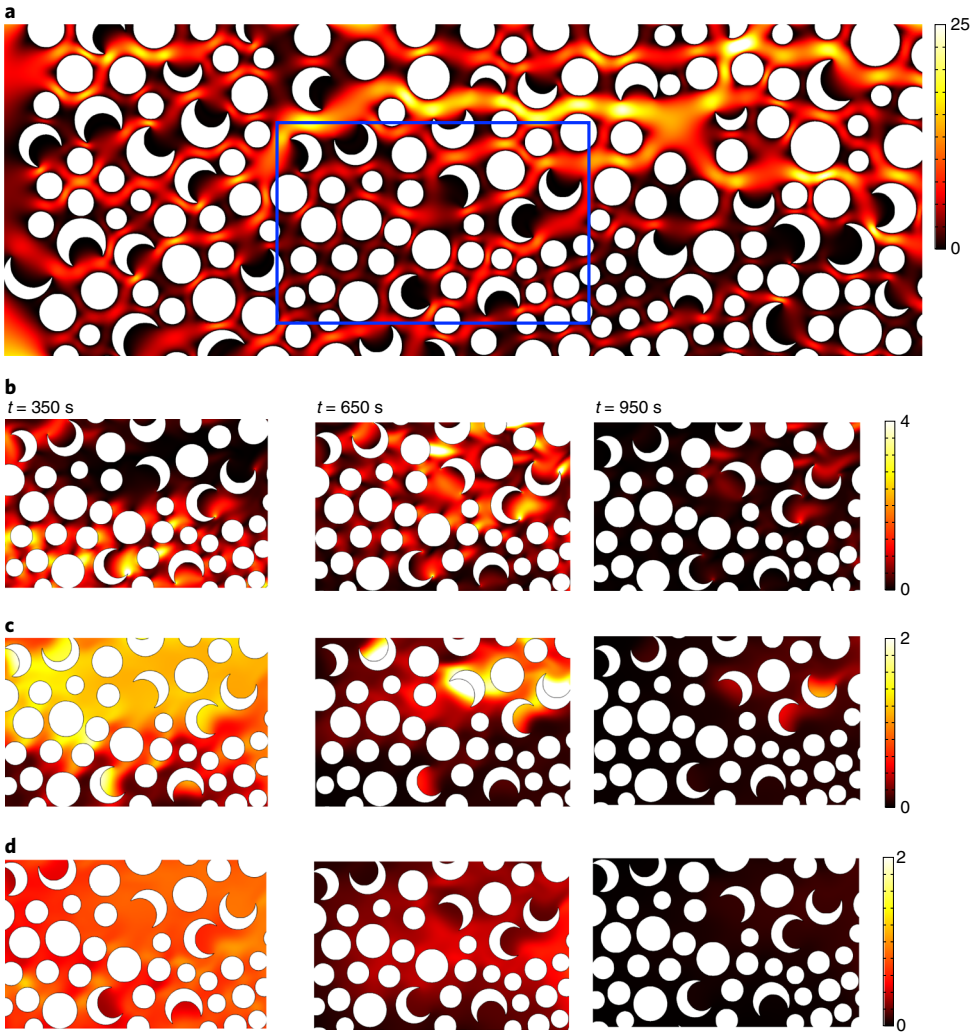


**Fig. 3 | Flow disorder maintains strong chemical gradients over long timescales. a**, The spatial map of flow Péclet number (Pe), showing high-Pe preferential flow paths together with low-Pe micropockets. **b**, Time evolution of the chemotactic Péclet number ($Pe_c$) over the selected low-flow area (blue rectangle in **a**), showing that regions with $Pe_c > 1$ persist much longer than the characteristic diffusion timescale of $\tau_D = 60$ s. **c**, Time evolution of bacterial density fields for chemorepellent injection. Micropockets with enhanced trapping or removal of the bacteria are correlated with the regions where $Pe_c > 1$ in **b**. The persistent chemical gradients are therefore strong enough to sustain chemotaxis over long timescales. **d**, Time evolution of bacterial density fields for chemoattractant injection, which leads to enhanced removal of bacteria from micropockets.

we conducted numerical simulations using a mathematical model of coupled flow, solute transport and bacterial chemotaxis in the microfluidic device (Supplementary Section VII). The injected sharp solute front is advected by the background flow field and becomes more diffuse as it travels along the device (Extended Data Figs. 7 and 9). This broadening of the solute front can be much larger than what molecular diffusion alone can cause, an effect commonly known as Taylor dispersion[36,37]. In a 1D setting such as flow in a rectilinear channel, the solute front width can be estimated as $\sqrt{D_{\mathrm{eff}}t}$; here, the effective dispersion coefficient can be written as $D_{\mathrm{eff}} = D_s(1 + \alpha \mathrm{Pe}^2)$ (refs. [36,37]), where $\alpha$ is a constant depending on the geometry, and the Péclet number $\mathrm{Pe} = U\lambda/D_s$ represents the ratio of advective to diffuse effects. In a disordered medium, low-velocity micropockets are surrounded by preferential flow paths where the Péclet number is high (Fig. 3a). This flow organization broadens the solute front[28,38] and is responsible for maintaining the solute gradients around the low-flow regions over long times (Supplementary Sections VII.E–F).

The chemical gradients, however, need to be sufficiently strong for chemotaxis to be relevant. To characterize the strength of the chemical gradients, we define the chemotactic Péclet number $\mathrm{Pe}_c = U_c\lambda/D_b$, which represents the ratio of chemotactic swimming to bacterial diffusion. We assume that the chemotactic swimming speed is linearly proportional to the solute concentration gradient $U_c = |\mathbf{u}_c| = |\kappa \nabla c|$, where $\kappa$ represents the strength of the chemotactic response and $c$ represents the solute concentration field[39,40] (Supplementary Sections VII.E–F). In regions where $\mathrm{Pe}_c > 1$, chemical gradients are sufficiently strong for chemotaxis to dominate over bacterial diffusion (Fig. 3b), leading to trapping of bacteria in the chemorepellent case (Fig. 3c) and enhanced removal of bacteria in the chemoattractant case (Fig. 3d). Taken together, these results demonstrate that, through its effect on the chemical concentration field, the pore-scale fluid physics creates strong gradients within the pores that directly affect the behaviour and spatio-temporal distribution of microorganisms at the pore scale.

To quantify the macroscale consequences of the pore-scale chemotactic migration of bacteria, we quantified the temporal evolution of the total bacterial biomass, $M_b$, over a region of ~400 pores (Extended Data Fig. 3 and Supplementary Section III), by using image coverage as proxy for bacterial mass. As the invading fluid

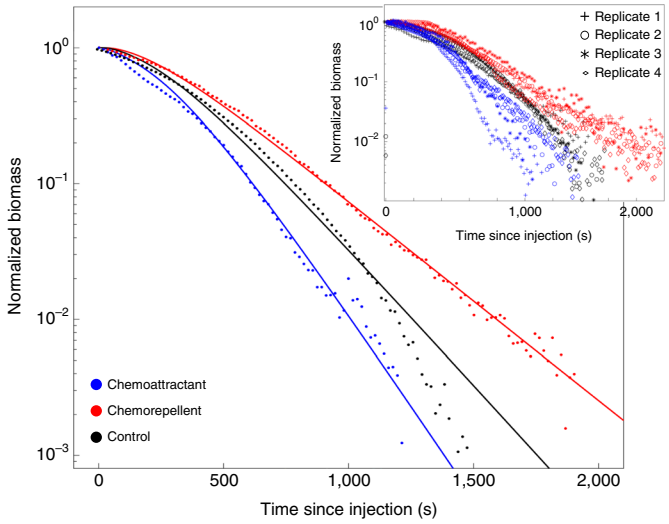


**Fig. 4 | Pore-scale chemotaxis causes system-scale changes in bacterial transport.** Shown is the temporal evolution of the total biomass $M_b$ in a 16-mm-long region of the porous medium, rescaled by the initial biomass, averaged over four replicates, following injection of a chemorepellent (red symbols), a chemoattractant (blue symbols) and the bacterial supernatant (control; black symbols). In the inset, different symbols indicate the four replicates of each experiment. In all cases, the bacterial population decreases as the invading fluid displaces the initial fluid. The evolution of the bacterial biomass is accurately captured by an advection–dispersion model, equation (2), with a single fitting parameter, the effective bacterial dispersion coefficient $D^*$. Chemotactic behaviour can considerably retard or accelerate this removal process, leading to a twofold difference in the effective dispersion coefficient between chemorepellent and chemoattractant injections.

displaces the defending suspension and progressively flushes out bacteria, $M_b$ decreases exponentially with time for both the chemoattractant, chemorepellent and control cases, as shown by the linear decrease in the semi-logarithmic plot in Fig. 4. Importantly, $M_b$ decreases much more slowly for a chemorepellent injection compared with a chemoattractant injection, with the no-gradient control case falling between the two (Fig. 4). This difference in the macroscale persistence time of bacterial biomass in the porous medium is consistent with the observed chemotactic behaviour of bacteria migrating into low-flow micropockets when the invading fluid is a chemorepellent and out of them when it is a chemoattractant. This observation, then, demonstrates that behaviour at the pore scale directly and measurably affects transport at the macroscale—an effect that is also captured by the numerical model (Extended Data Fig. 10). The agreement between simulations and experiments is only qualitative, and this can be the result of several assumptions and approximations made in our mathematical model (Supplementary Section VII.D), including having considered a 2D flow field, whereas in reality the medium is 3D, having assumed that the chemotactic velocity is a linear function of the concentration gradient and considering the chemotactic strength to be independent of the local solute concentration[41,42].

The effect of chemotaxis on macroscale transport can be quantified by comparison with an advection–dispersion model (Supplementary Section VI). The model predicts the cross-sectional average concentration of bacteria $\bar{n}(x,t)$ along the flow direction $x$ following the sudden arrival of an invading fluid at time $t=0$. The solution of the advection–dispersion model yields[43]:

$$\bar{n}(x,t) = \frac{\bar{n}_0}{2}\left[1 + \mathrm{erf}\left(\frac{x-Ut}{\sqrt{D^*t}}\right)\right] \quad (1)$$

where $U = 0.026\,\mathrm{mm\,s^{-1}}$ is the average longitudinal velocity within the porous medium (Supplementary Section II.B), $\bar{n}_0$ is the initial concentration of bacteria prior to invasion and $D^*$ is the effective dispersion coefficient. Integrating $\bar{n}(x,t)$ over the 16-mm-long observation region provides a prediction of the total biomass $M_b$ in that region at time $t$:

$$\begin{aligned} M_b(t) &= \frac{\bar{n}_0}{2}\left[x + (x-Ut)\,\mathrm{erf}\left(\frac{x-Ut}{\sqrt{D^*t}}\right) + \frac{\sqrt{D^*t}\,\exp\left(-\frac{(x-Ut)^2}{D^*t}\right)}{\sqrt{\pi}}\right]_{x=0}^{x=L} \\ &\sim \exp\left(-\frac{t}{\tau^*}\right) \quad \text{for } t > \tau^* = D^*/U^2 \end{aligned} \quad (2)$$

where $\sim$ denotes proportionality. This prediction captures the observed decrease in biomass at all times (Fig. 4). In particular, the final expression in equation (2) emphasizes that at long times ($t > \tau^* = D^*/U^2$) the biomass decays exponentially in time, in agreement with the observations. In our experiments, all quantities in equation (2) are known except for $D^*$, enabling the quantification of the decay timescale $\tau^*$ by fitting the predicted late-time exponential decay to the experimental data (Fig. 4). This results in decay timescales of $\tau^*_{\mathrm{repell}} = 360\,\mathrm{s}$, $\tau^*_{\mathrm{attract}} = 180\,\mathrm{s}$ and $\tau^*_{\mathrm{control}} = 210\,\mathrm{s}$ (four replicates for each case). Because the average fluid velocity $U$ was the same in all experiments, the same relative differences among the two invading solutions and the no-gradient control apply to the longitudinal dispersion coefficient $D^*$ ($=\tau^* U^2$). These results demonstrate that chemotaxis away from an invading chemorepellent or towards an invading chemoattractant, respectively, retarded or accelerated the flushing of bacteria from the porous medium, with an overall twofold difference in the biomass decay timescale.

The effect of chemotaxis reported here can be distilled into a quantification of the effective dispersion coefficient of the bacterial suspension, for use in future models of bacterial transport. The observed biomass decay times directly yield estimates of the effective dispersion coefficient $D^* = \tau^* U^2$, resulting in $D^*_{\mathrm{repell}} = 0.196 \pm 0.004\,\mathrm{mm^2\,s^{-1}}$ for the invading chemorepellent solution, $D^*_{\mathrm{attract}} = 0.108 \pm 0.002\,\mathrm{mm^2\,s^{-1}}$ for the invading chemoattractant solution and $D^*_{\mathrm{control}} = 0.145 \pm 0.003\,\mathrm{mm^2\,s^{-1}}$ for the no-gradient control. The twofold difference in the effective dispersion coefficient between attraction and repulsion results in a 6.2-fold decrease in late-time biomass ($\exp[D^*_{\mathrm{repell}}/D^*_{\mathrm{attract}}]$), highlighting the considerable macroscale impact of chemotaxis on the transport (here, removal) of bacteria in a porous medium.

Classical descriptions of transport in porous media have relied on the advection–dispersion framework[33], where the coefficient of hydrodynamic dispersion is tasked with capturing unresolved flow heterogeneity. Although the dispersion coefficient can be adjusted to fit the macroscopic response, by itself it offers no connection to the underlying mechanisms responsible for microbial dispersion. Here we have shown that in the case of chemical flushing of chemotactic bacteria, this connection rests on the enhanced longitudinal dispersion of moving chemical fronts associated with shear and flow disorder inherent to porous media[36,38]. At the pore scale, the broadened chemical fronts cause long-lived strong chemical gradients, which in turn can have major direct consequences on biological transport, as captured by large changes in the effective dispersion coefficient and the resident biomass. Although other mechanisms—such as population fluctuations[44] or geometry of the pore space[45]—can also lead to bacterial accumulation in tight spaces, we do not think that they play a role in our experiments because we consider non-growing microbes and our pores are approximately symmetric and two orders of magnitude larger than a single bacterium.

Although in open flows, such as in the ocean, the complex and filamentary structure of nutrients is a product of the turbulent nature of the fluid, in porous media the velocity disorder emerges

from the organization of flow into high-velocity paths and stagnation zones, in the absence of any turbulence or inertial effects. Given the ubiquity of flow disorder in natural porous media like soils and rocks and the generality of our model system, we anticipate that the fundamental mechanisms uncovered here from high-resolution experiments and numerical simulations in analogue porous media built on microfluidics devices will translate to a broad range of microbial species in natural subsurface environments. The interplay between chemical transport at the pore scale and the chemotactic response is thus likely to have a major impact on microbially mediated biogeochemical processes like contaminant bioremediation, remineralization, element cycling and ecosystem stability.

## Online content

Any methods, additional references, Nature Research reporting summaries, source data, extended data, supplementary information, acknowledgements, peer review information; details of author contributions and competing interests; and statements of data and code availability are available at https://doi.org/10.1038/s41567-020-1002-x.

Received: 30 January 2019; Accepted: 10 July 2020;
Published online: 14 September 2020

## References

1. Whitman, W. B., Coleman, D. C. & Wiebe, W. J. Prokaryotes: the unseen majority. *Proc. Natl Acad. Sci. USA* **95**, 6578–6583 (1998).
2. Torsvik, V., Øvreås, L. & Thingstad, T. F. Prokaryotic diversity—magnitude, dynamics and controlling factors. *Science* **296**, 1064–1066 (2002).
3. Chivian, D. et al. Environmental genomics reveals a single-species ecosystem deep within earth. *Science* **322**, 275–278 (2008).
4. McClain, M. E. et al. Biogeochemical hot spots and hot moments at the interface of terrestrial and aquatic ecosystems. *Ecosystems* **6**, 301–312 (2003).
5. Tebo, B. M. et al. Biogenic manganese oxides: properties and mechanisms of formation. *Annu. Rev. Earth Planet. Sci.* **32**, 287–328 (2004).
6. Or, D., Smets, B. F., Wraith, J. M., Dechesne, A. & Friedman, S. P. Physical constraints affecting bacterial habitats and activity in unsaturated porous media—a review. *Adv. Water Resour.* **30**, 1505–1527 (2007).
7. Grathwohl, P. et al. Catchments as reactors: a comprehensive approach for water fluxes and solute turnover. *Environ. Earth Sci.* **69**, 317–333 (2013).
8. Olson, M. S., Ford, R. M., Smith, J. A. & Fernandez, E. J. Quantification of bacterial chemotaxis in porous media using magnetic resonance imaging. *Environ. Sci. Technol.* **38**, 3864–3870 (2004).
9. Wang, M. & Ford, R. M. Transverse bacterial migration induced by chemotaxis in a packed column with structured physical heterogeneity. *Environ. Sci. Technol.* **43**, 5921–5927 (2009).
10. Strobel, K. L. et al. Chemotaxis increases vertical migration and apparent transverse dispersion of bacteria in a bench-scale microcosm. *Biotechnol. Bioeng.* **108**, 2070–2077 (2011).
11. Blackburn, N., Fenchel, T. & Mitchell, J. Microscale nutrient patches in planktonic habitats shown by chemotactic bacteria. *Science* **282**, 2254–2256 (1998).
12. Stocker, R. Marine microbes see a sea of gradients. *Science* **338**, 628–633 (2012).
13. Szurmant, H. & Ordal, G. W. Diversity in chemotaxis mechanisms among the bacteria and archaea. *Microbiol. Mol. Biol. Rev.* **68**, 301–319 (2004).
14. Abraham, E. R. The generation of plankton patchiness by turbulent stirring. *Nature* **391**, 577–580 (1998).
15. Tél, T., de Moura, A., Grebogi, C. & Károlyi, G. Chemical and biological activity in open flows: a dynamical system approach. *Phys. Rep.* **413**, 91–196 (2005).
16. Taylor, J. R. & Stocker, R. Trade-offs of chemotactic foraging in turbulent water. *Science* **338**, 675–679 (2012).
17. de Anna, P. et al. Mixing and reaction kinetics in porous media: an experimental pore scale quantification. *Environ. Sci. Technol.* **48**, 508–516 (2014).
18. de Anna, P., Quaife, B., Biros, G. & Juanes, R. Prediction of the low-velocity distribution from the pore structure in simple porous media. *Phys. Rev. Fluids* **2**, 124103 (2017).
19. Long, T. & Ford, R. M. Enhanced transverse migration of bacteria by chemotaxis in a porous T-sensor. *Environ. Sci. Technol.* **43**, 1546–1552 (2009).
20. Singh, R. & Olson, M. S. Transverse mixing enhancement due to bacterial random motility in porous microfluidic devices. *Environ. Sci. Technol.* **45**, 8780–8787 (2011).
21. Duffy, K. J., Ford, R. M. & Cummings, P. T. Residence time calculation for chemotactic bacteria within porous media. *Biophys. J.* **73**, 2930–2936 (1997).
22. Ebrahimi, A. N. & Or, D. Microbial dispersal in unsaturated porous media: characteristics of motile bacterial cell motions in unsaturated angular pore networks. *Water Resources Res.* **50**, 7406–7429 (2014).
23. Adadevoh, J. S., Triolo, S. C., Ramsburg, C. A. & Ford, R. M. Chemotaxis increases the residence time of bacteria in granular media containing distributed contaminant sources. *Environ. Sci. Technol.* **50**, 181–187 (2016).
24. Adadevoh, J. S., Ostvar, S., Wood, B. & Ford, R. M. Modeling transport of chemotactic bacteria in granular media with distributed contaminant sources. *Environ. Sci. Technol.* **51**, 14192–14198 (2017).
25. Wang, M., Lanning, L. & Ford, R. M. Enhanced retention of chemotactic bacteria in a pore network with residual NAPL contamination. *Environ. Sci. Technol.* **50**, 165–172 (2016).
26. Porter, M. L., Valdés-Parada, F. J. & Wood, B. D. Multiscale modeling of chemotaxis in homogeneous porous media. *Water Resour. Res.* **47**, W06518 (2011).
27. Datta, S. S., Chiang, H., Ramakrishnan, T. S. & Weitz, D. A. Spatial fluctuations of fluid velocities in flow through a three-dimensional porous medium. *Phys. Rev. Lett.* **111**, 064501 (2013).
28. Kang, P. K. et al. Pore-scale intermittent velocity structure underpinning anomalous transport through 3-D porous media. *Geophys. Res. Lett.* **41**, 6184–6190 (2014).
29. de Anna, P. et al. Flow intermittency, dispersion and correlated continuous time random walks in porous media. *Phys. Rev. Lett.* **110**, 184502 (2013).
30. Holzner, M., Morales, V. L., Willmann, M. & Dentz, M. Intermittent Lagrangian velocities and accelerations in three-dimensional porous medium flow. *Phys. Rev. E* **92**, 013015 (2015).
31. Rusconi, R., Garren, M. & Stocker, R. Microfluidics expanding the frontiers of microbial ecology. *Annu. Rev. Biophys.* **43**, 65–91 (2014).
32. Hol, F. J. H. & Dekker, C. Zooming in to see the bigger picture: microfluidic and nanofabrication tools to study bacteria. *Science* **346**, 1251821 (2014).
33. Bear, J. *Dynamics of Fluids in Porous Media* (Elsevier, 1972).
34. Yawata, Y. et al. Competition–dispersal trade-off ecologically differentiates recently speciated marine bacterioplankton populations. *Proc. Natl Acad. Sci. USA* **111**, 5622–5627 (2014).
35. Kim, J. et al. Hydrodynamic effects on bacterial biofilm development in a microfluidic environment. *Lab Chip* **13**, 1846–1849 (2013).
36. Taylor, G. I. Dispersion of soluble matter in solvent flowing slowly through a tube. *Proc. R. S. Lond. A Math. Phys. Sci.* **219**, 186–203 (1953).
37. Squires, T. M. & Quake, S. R. Microfluidics: fluid physics at the nanoliter scale. *Rev. Mod. Phys.* **77**, 977–1026 (2005).
38. Sahimi, M. Flow phenomena in rocks: from continuum models to fractals, percolation, cellular automata and simulated annealing. *Rev. Mod. Phys.* **65**, 1393–1534 (1993).
39. Keller, E. F. & Segel, L. A. Model for chemotaxis. *J. Theor. Biol.* **30**, 225–234 (1971).
40. Tuval, I. et al. Bacterial swimming and oxygen transport near contact lines. *Proc. Natl Acad. Sci. USA* **102**, 2277–2282 (2005).
41. Lazova, M. D., Ahmed, T., Bellomo, D., Stocker, R. & Shimizu, T. S. Response rescaling in bacterial chemotaxis. *Proc. Natl Acad. Sci. USA* **108**, 13870–13875 (2011).
42. Wang, M., Atencia, J. & Ford, R. M. Quantitative analysis of chemotaxis towards toluene by *Pseudomonas putida* in a convection-free microfluidic device. *Biotechnol. Bioeng.* **112**, 896–904 (2015).
43. Crank, J. *Mathematics of Diffusion* 2nd edn (Oxford Univ. Press, 1975).
44. Park, S. et al. Influence of topology on bacterial social interaction. *Proc. Natl Acad. Sci. USA* **100**, 13910–13915 (2005).
45. Galajda, P. et al. Funnel ratchets in biology at low Reynolds number: choanotaxis. *J. Mod. Opt.* **55**, 3412–3422 (2008).

## Methods

**Bacterial isolates and cell cultures.** The bacterial strains used in this study are *B. subtilis* sp. OI1085 wild type. For routine culture, bacterial strains were grown in Luria Bertani liquid medium at 37 °C in an orbital shaker (550 r.p.m.). For every experiment, the microbial culture was left to grow overnight under these conditions, and was then washed and separated from the spent medium before being resuspended in a PBS solution (Sigma-Aldrich) with a predetermined concentration of tryptone (described below). The washing procedure for the microbial suspensions consisted of the following steps: (1) collect 1 ml of a microbial culture in its mid-exponential growth phase and centrifuge it at 3.0 relative centrifugal field (RCF); (2) remove the supernatant (spent medium), keeping the solid phase compact and deposited at the bottom of the tube; (3) add 1 ml of PBS solution of tryptone at 0.5% and mix it until the solid aggregate of microbes is homogeneously resuspended; (4) place the 1 ml of washed suspension in an orbital shaker for 30 min.

**Image acquisition and analysis for microbial displacement at the invading front.** We set the microscope (a fully automated Nikon Ti-E) and the camera (Andor Zyla 5.5) to capture one large image every 17 s, saving greyscale pictures as PNG files with 12-bit pixel depth. We performed the experiments with ×6 magnification. A large image was composed of 12 pictures (two rows of six pictures each), so that the total field of view was ~10.8 mm × 4.6 mm, corresponding to ~8 × 50 average pore sizes (Supplementary Fig. 5). Greyscale pictures were taken with phase contrast microscopy using a Nikon ×4 Plan Fluor Ph1 objective (and an internal scope of ×1.5, giving the final ×6 magnification) in combination with a phase ring Ph3 (of size larger than the ring present in the selected objective) so that the sample was illuminated almost laterally, thereby obtaining pictures in which the background was dark and bacteria were detected as objects scattering light, appearing bright. With this configuration, we simultaneously detected the position of individual bacteria as well as the porous landscape of ~8 × 50 = 400 pores of different size and shape where microbes could be transported by the flow or trapped. For each experiment, we took 120 images for a total duration of ~40 min.

**Fluorescent tracer as a transport analogue of tryptone.** Because we cannot directly measure the local concentration of the chemoattractant, we used fluorescein sodium salt (Sigma-Aldrich) as tracer analogue, which has a molecular weight of 376 and a diffusion coefficient in water of $\sim 7 \times 10^{-10}\,m^2\,s^{-1}$ at 20 °C. This is very similar to the diffusion coefficient of the chemoattractant tryptone. The latter was estimated to $7 \times 10^{-10}\,m^2\,s^{-1}$ by considering that tryptone is mostly (>92%) composed of small amino acids, including tryptophan, lysin and phenylalanine, whose diffusion coefficient falls in the range $6 \times 10^{-10}\,m^2\,s^{-1}$ to $8 \times 10^{-10}\,m^2\,s^{-1}$. The technique we describe below provides a dynamical quantification of the spatial distribution of concentration down to ~1% of the injected concentration value. We used video microscopy to image the signal emitted by the incoming fluorescent tracer (~515 nm) while stimulated by a light source (~460 nm) embedded in the microscope. The number of photons emitted by the irradiated fluorescent tracer is proportional to the number of its stimulated molecules, that is, to its mass. The light coming from the microfluidics device was filtered before being detected by the camera to remove photons that are not emitted by the tracer, but are already present in the exciting irradiation and the laboratory environment. By taking pictures of the invading tracer, we inferred its concentration from the measured light intensity detected by each pixel via a calibration procedure (Supplementary Section V.A).

**Implementation of the numerical model of bacterial chemotaxis.** In Supplementary Section VII, we describe a mathematical model of coupled flow, solute transport and bacterial chemotaxis, which helps elucidate the mechanisms underlying the observed trends in bacterial retention in our experiments. The governing equations were solved using COMSOL Multiphysics software. The Stokes equations describing steady fluid flow through the 2D microfluidic device were solved using the finite element method on a triangular mesh with linear elements. The unsteady advection–diffusion equations for the solute and bacterial concentration fields were then also solved using the finite element method with linear elements and the default stabilization in COMSOL. The time stepping employed backward differentiation formulae (BDF) with automatic time-step size. The linear system of equations at each time step was solved using a direct solver algorithm. We used an extremely fine unstructured triangular mesh (~1,250,000 elements), ensuring that the tight pore spaces and sharp corners were captured accurately and that the solution did not depend on mesh size.

**Reporting Summary.** Further information on research design is available in the Nature Research Reporting Summary linked to this Article.

## Data availability

Additional data that support the plots within this Paper and other findings of this study are available at the Zenodo repository (https://doi.org/10.5281/zenodo.3926720). Source data are provided with this paper.

## Code availability

The algorithms and simulation codes are described in the Methods and Supplementary Information.

## Acknowledgements

P.d.A. acknowledges the Earth Resource Laboratory of the Massachusetts Institute of Technology for the ERL fellowship that supported this research. R.J. acknowledges funding from the US Department of Energy (grant no. DE-SC0018357). R.S. acknowledges support from the Swiss National Science Foundation (grant no. 315230_176189).

## Author contributions

P.d.A., R.S. and R.J. designed the research. P.d.A. and A.A.P. performed the research. Y.Y. contributed with chemotaxis steady experiments. P.d.A. and A.A.P. analysed data. P.d.A., A.A.P., Y.Y., R.S. and R.J. wrote the manuscript.

## Competing interests

The authors declare no competing interests.

## Additional information

**Extended data** is available for this paper at https://doi.org/10.1038/s41567-020-1002-x.

**Supplementary information** is available for this paper at https://doi.org/10.1038/s41567-020-1002-x.

**Correspondence and requests for materials** should be addressed to R.S. or R.J.

**Peer review information** *Nature Physics* thanks Yohan Davit and the other, anonymous, reviewer(s) for their contribution to the peer review of this work.

**Reprints and permissions information** is available at www.nature.com/reprints.

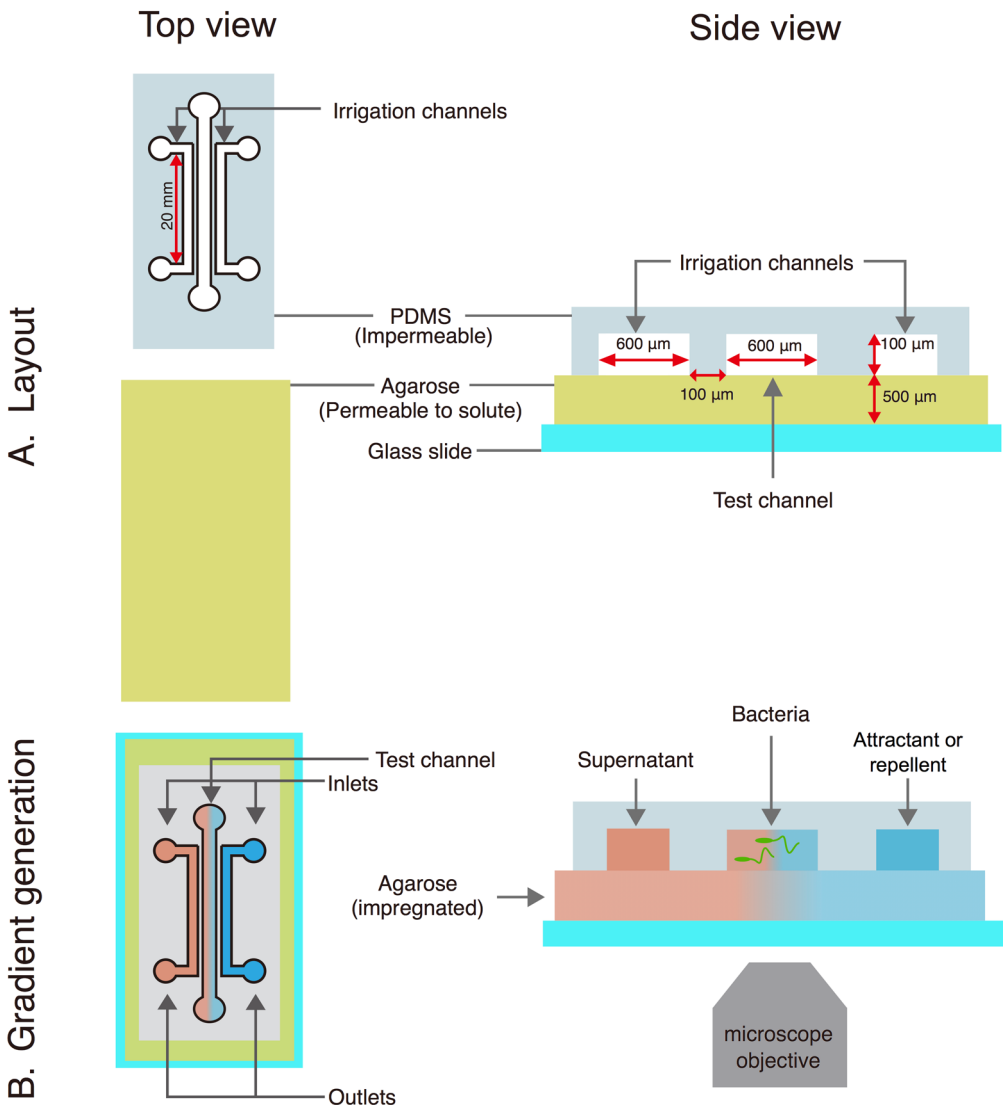


**Extended Data Fig. 1 | Schematic of the gradient generator used to assay chemotaxis in steady, linear chemoattractant profiles.** Schematic of the gradient generator used to assay chemotaxis in steady, linear chemoattractant profiles (adapted from ref. [34]). **a**, Schematic of the cross-section of the assembled device (right) and top view of each layer (left). The top layer is made of PDMS, which is impermeable to solutes. The middle layer is made of agarose, which allows for the diffusion of chemoattractant used to establish the linear concentration profile. The bottom layer is a glass slide, used for structural support. Solid red arrows denote dimensions. **b**, Schematic of the gradient-generation mechanism. The continuous flow of chemoattractant (red) and filtered autoclaved seawater (blue) within the two irrigation channels in the PDMS layer mediates the formation of a horizontal gradient (red-blue shading) in the underlying agarose layer and therefore in the test channel.

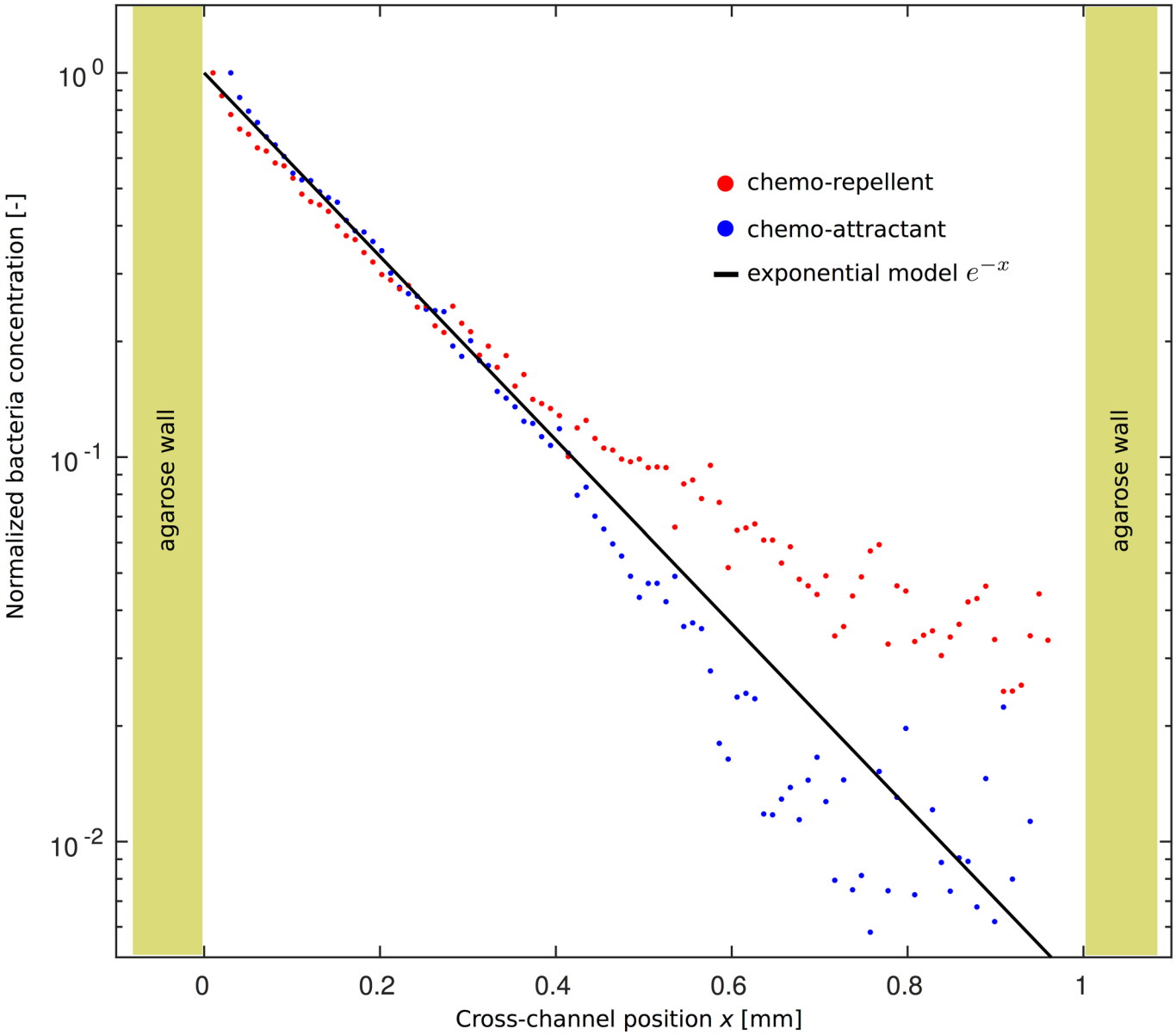


**Extended Data Fig. 2 | Spatial distribution of bacteria in the steady chemotaxis characterization experiment.** Spatial distribution of bacteria in the steady chemotaxis characterization experiment. The semi-logarithmic plot shows the average concentration of microbes along the negative-gradient direction. The linear trend indicates an exponential decay of the microbe concentration with distance from the attractant source and from the repellent sink (tryptone solution blue, spent medium red).

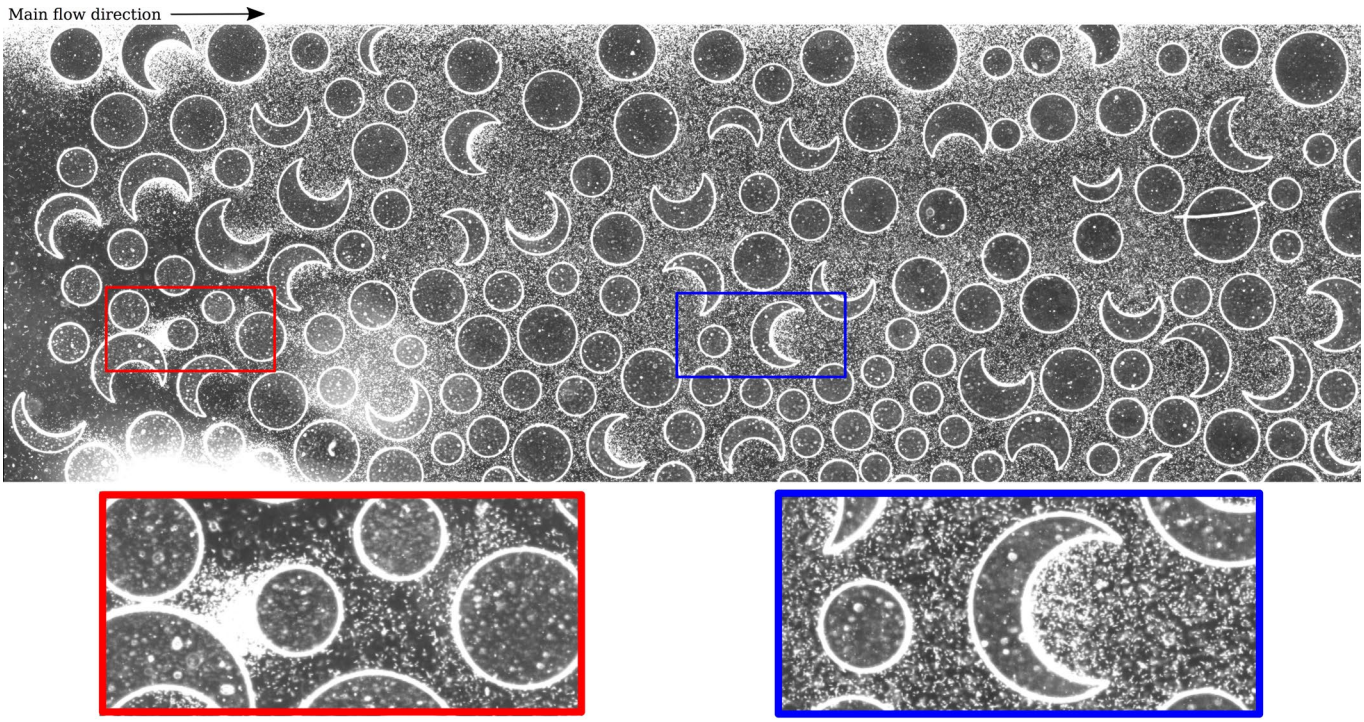


**Extended Data Fig. 3 | Large image of the microbes' position at 6X magnification.** Large image of the microbes' position at 6X magnification. The image is obtained as a composition of 2 × 6 individual pictures, using a phase contrast optical configuration. Individual microbes appear as white spots on a dark background, while larger circles and crescents are the vertical obstacles, mimicking the grains of a porous medium, which shape the flow heterogeneity in the microfluidics channel. Flow is from left to right.

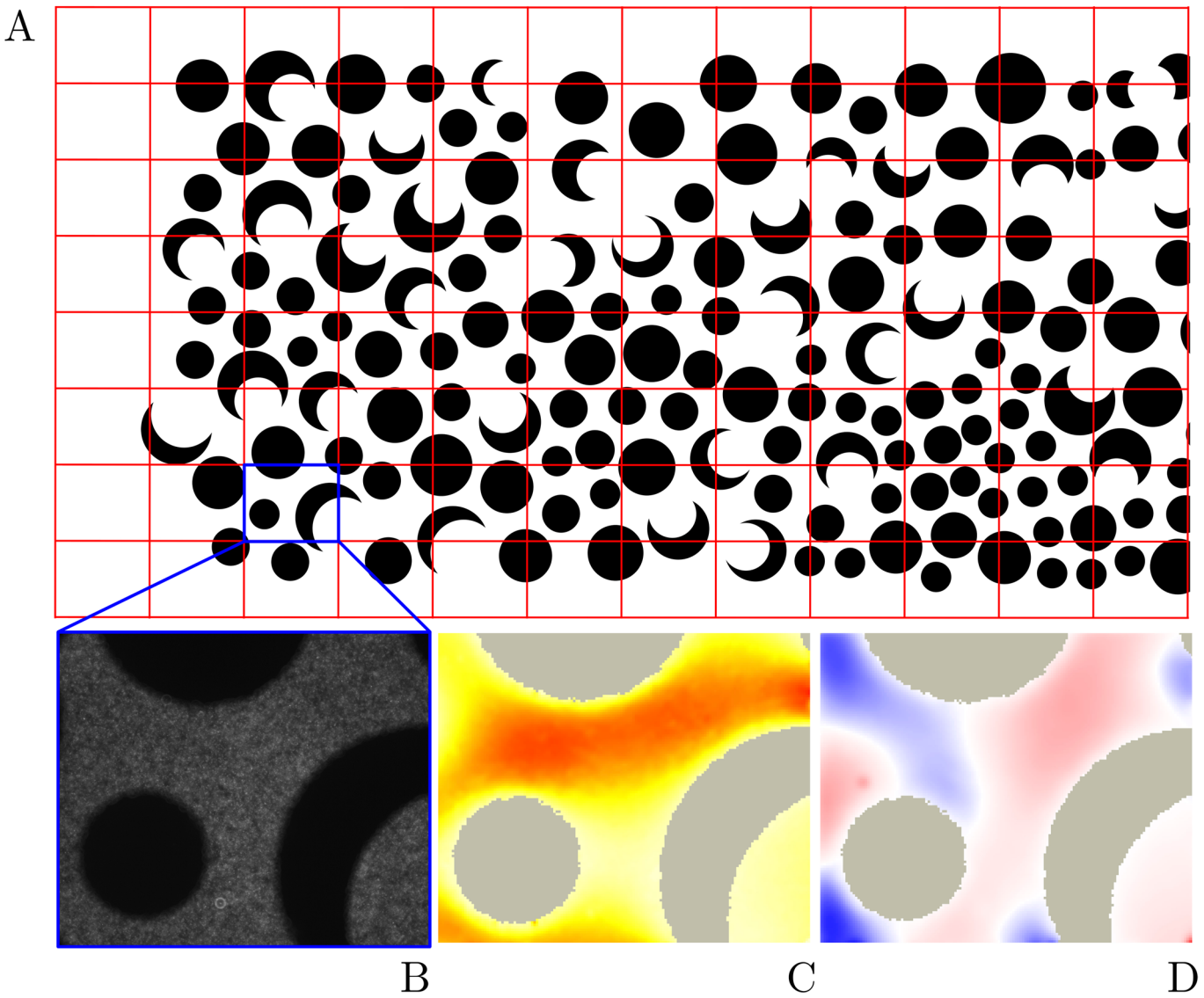


**Extended Data Fig. 4 | Measurement of the velocity field in the microfluidics flow cell.** Measurement of the velocity field in the microfluidics flow cell. **a**, Schematic of the spatial partition of the visible portion of the porous medium into tiles that are individually imaged and, then, analyzed with Particle Image Velocimetry. **b**, Fluorescent microspheres are suspended in the flow to seed the fluid and quantify its motion. **c,d**, Longitudinal and transverse velocity fields, respectively, in the same tile as (**b**).

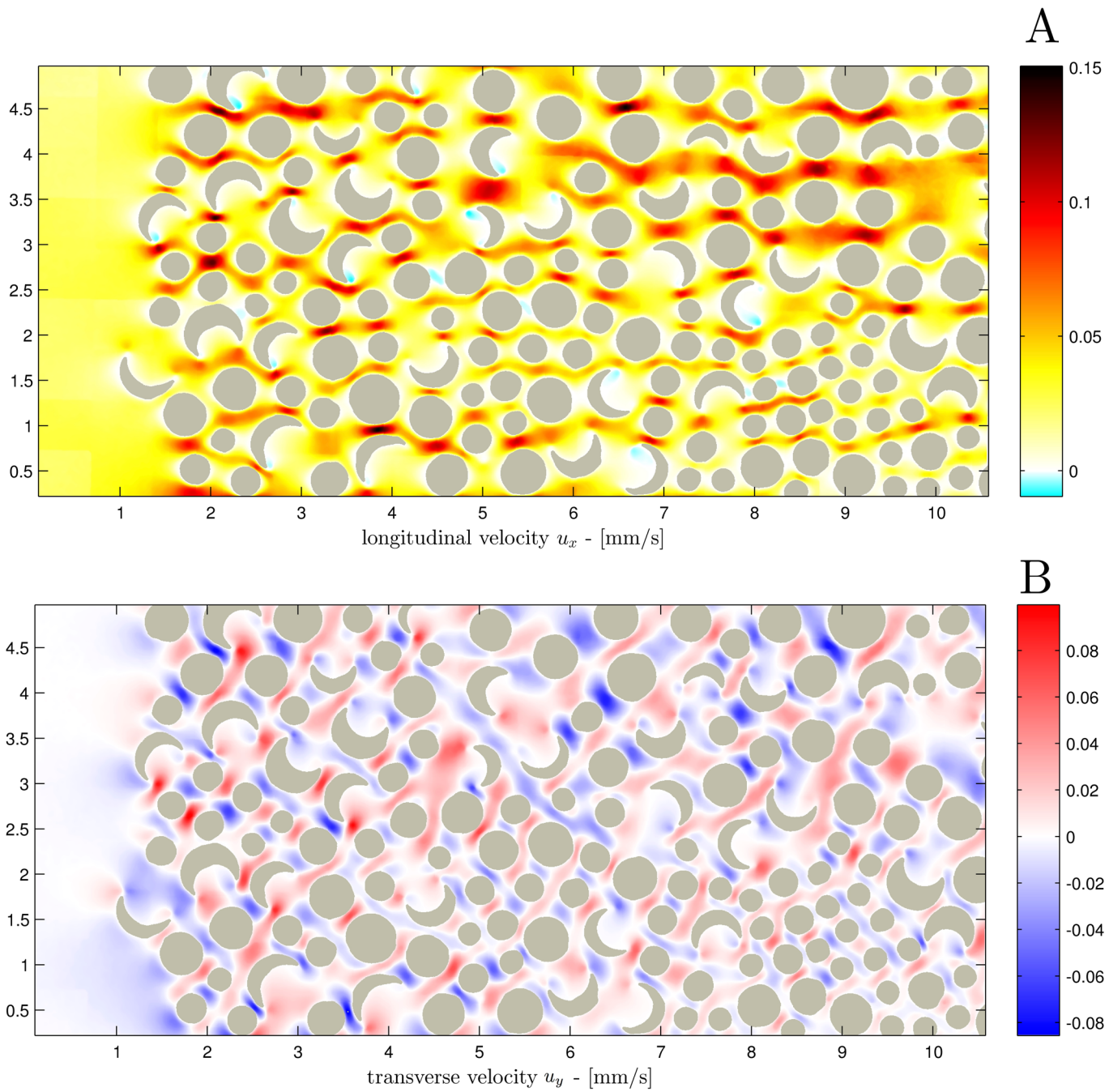


**Extended Data Fig. 5 | Velocity field over the entire porous medium.** Velocity field over the entire porous medium. **a,b**, Longitudinal and transverse velocity fields, respectively, obtained by collecting the PIV results of each tile in which the whole medium has been partitioned. The color maps are set to obtain white color where the fluid velocity is zero, dark-red where the velocity is positive, and dark-blue where it is negative.

t = 90 s

t = 185 s

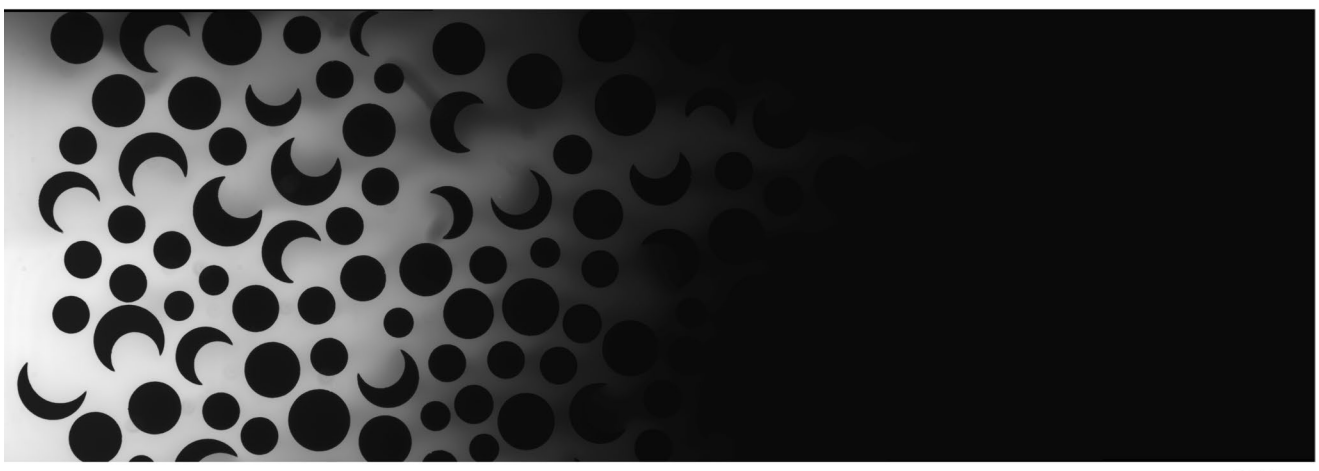

t = 262 s

RAW images of fluorescent tracer

**Extended Data Fig. 6 | Results of the tracer transport/mixing experiment showing the signal detected from the emission of the invading fluorescent tracer at three different times (t= 90 s, 185 s and 262 s).** Results of the tracer transport/mixing experiment showing the signal detected from the emission of the invading fluorescent tracer at three different times (t= 90 s, 185 s and 262 s).

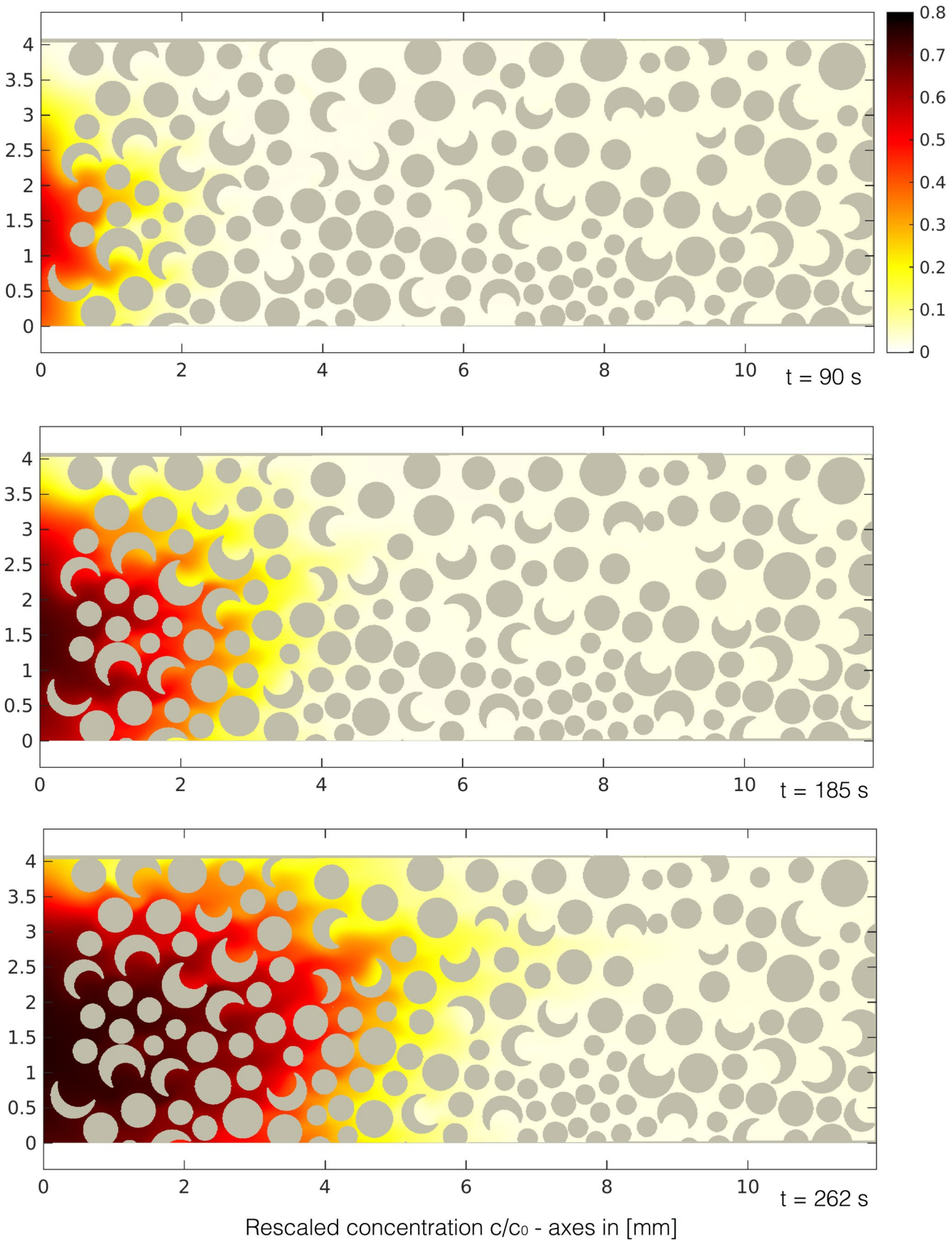


**Extended Data Fig. 7 | Results of the tracer transport/mixing experiment showing the concentration field that results from applying the calibration curve at three different times (t= 90 s, 185 s and 262 s).** Results of the tracer transport/mixing experiment showing the concentration field that results from applying the calibration curve at three different times (t= 90 s, 185 s and 262 s).

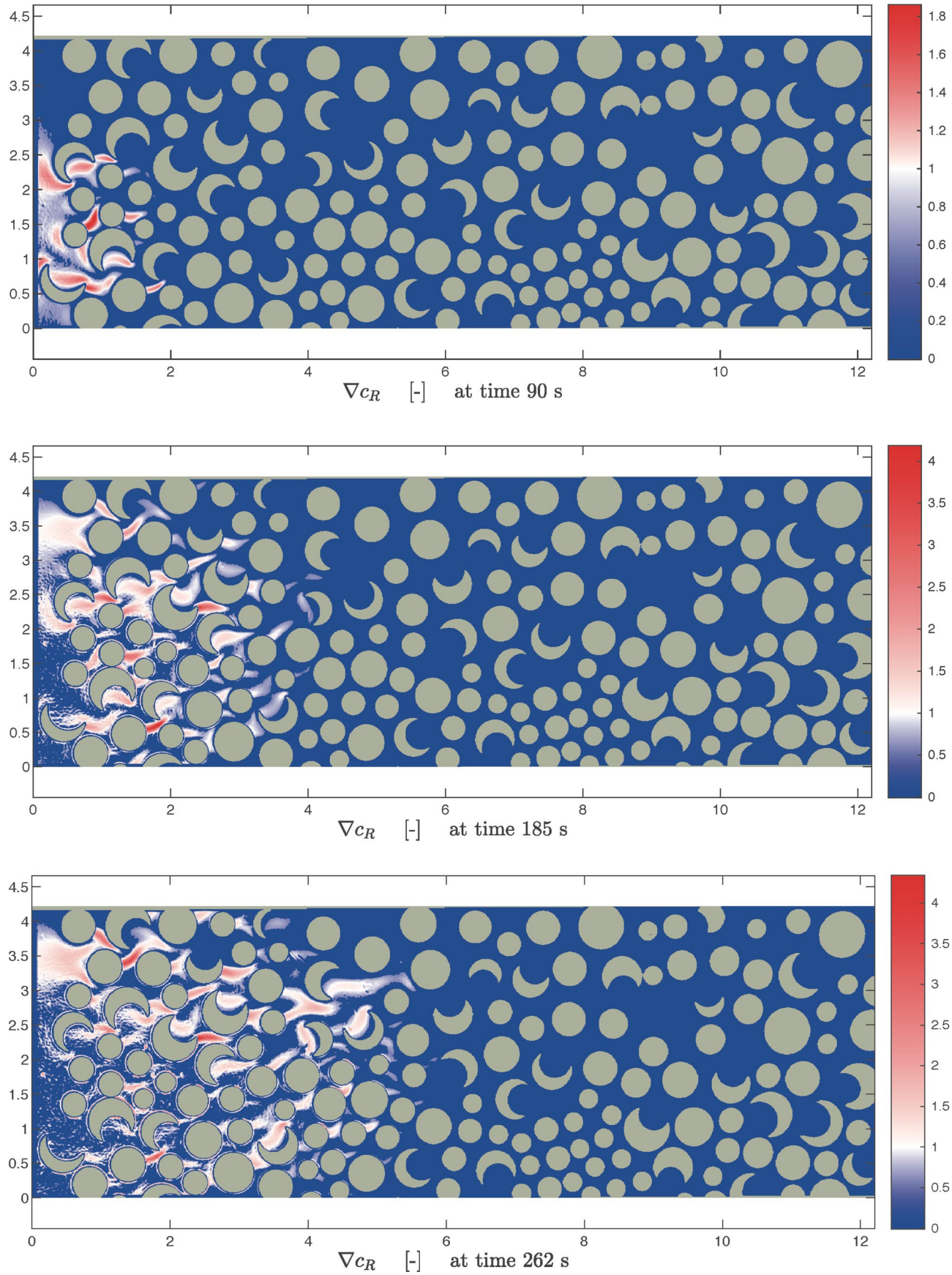


**Extended Data Fig. 8 | Results of the tracer transport/mixing experiment showing the rescaled concentration gradient field at three different times (t= 90 s, 185 s and 262 s).** Results of the tracer transport/mixing experiment showing the rescaled concentration gradient field at three different times (t= 90 s, 185 s and 262 s).

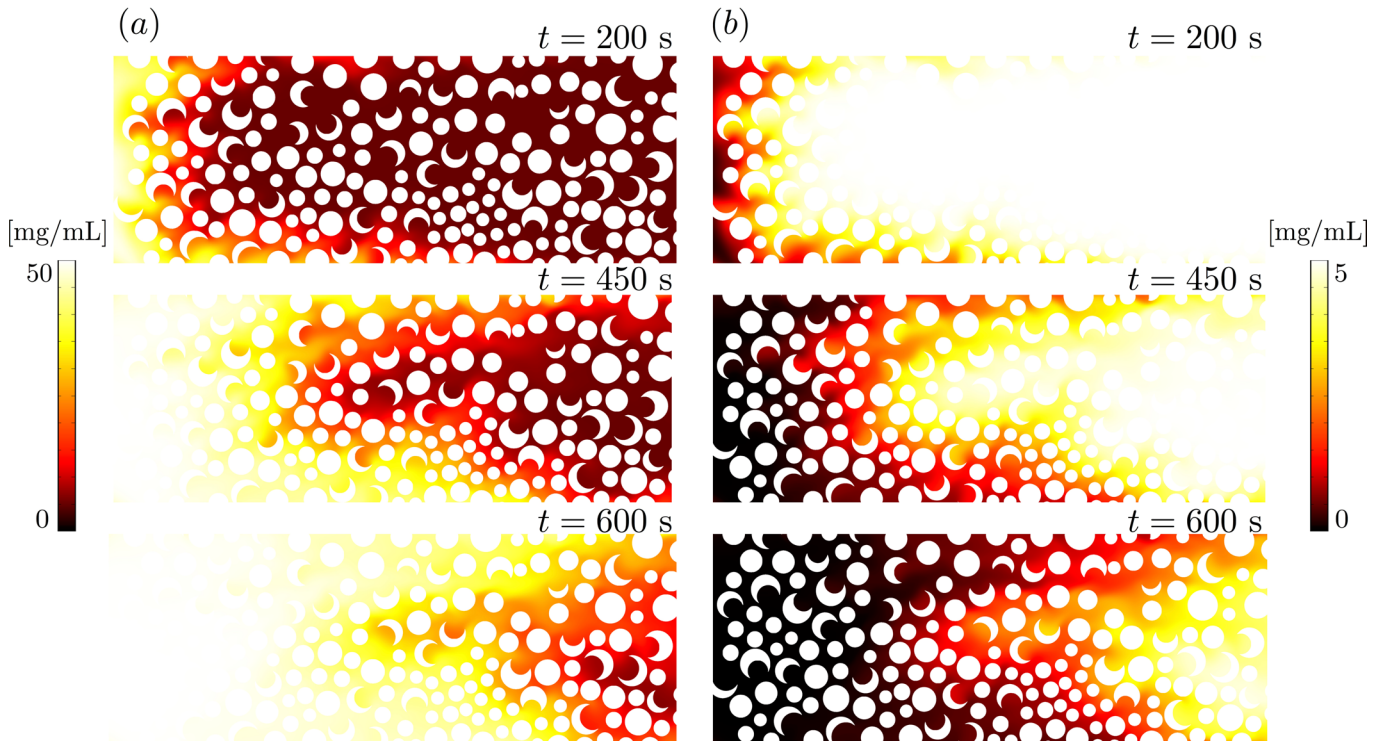


**Extended Data Fig. 9 | The evolution of solute concentration field from the numerical model.** The evolution of solute concentration field from the numerical model for (**a**) the chemoattractant case, and (**b**) the chemorepellent case. In both cases, the concentration of solute in the medium is initially set at c(t=0) = 5 mg/mL. A higher concentration c = 50 mg/mL is injected in the chemoattractant case, whereas a lower concentration c = 0 mg/mL is injected in the chemorepellent case.

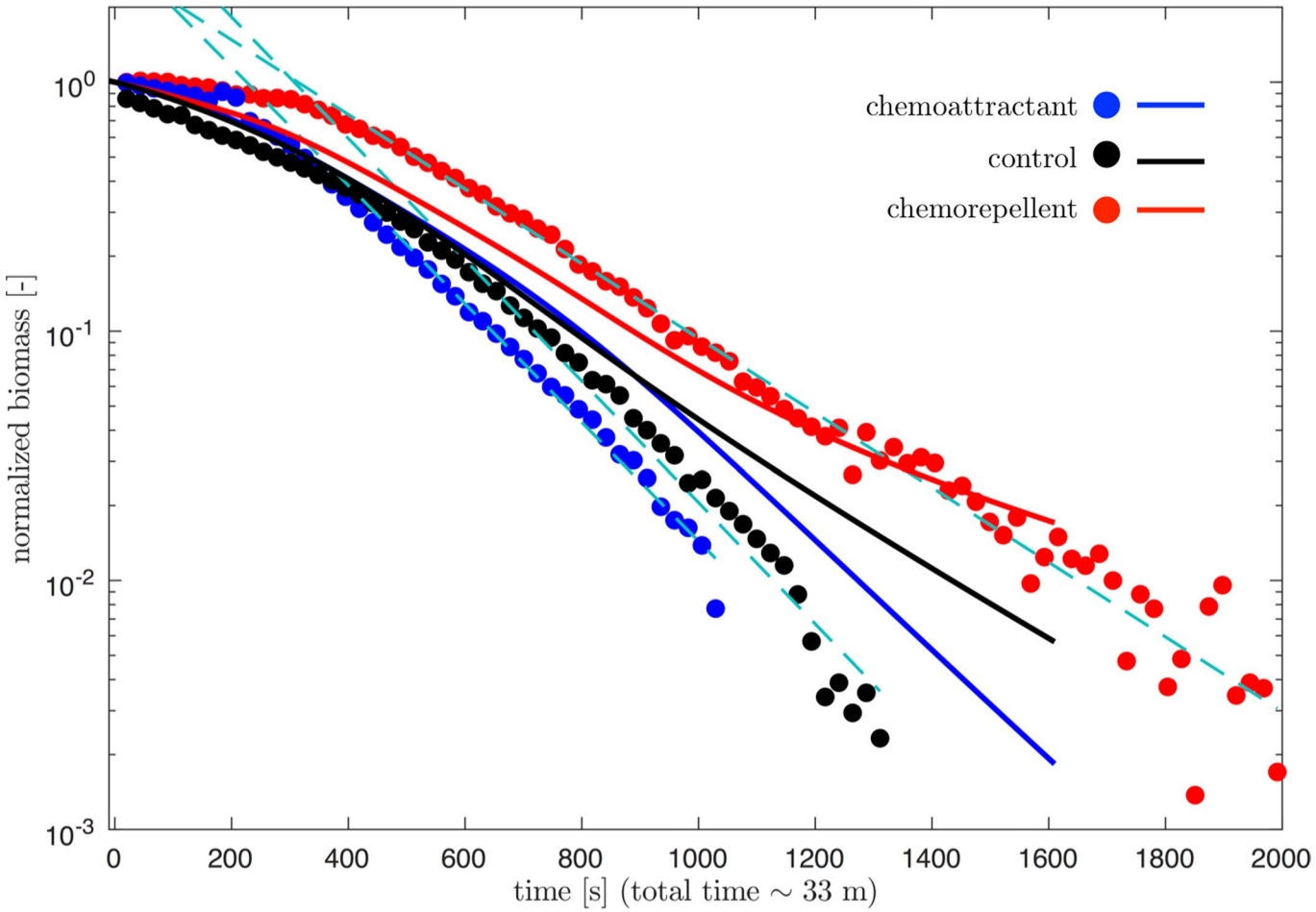


**Extended Data Fig. 10 | The evolution of normalized bacterial biomass in time.** The evolution of normalized bacterial biomass in time. Symbols represent the mean of the four experimental realizations, and solid lines represent the simulation results. The dashed lines represent the exponential fits to the experimental data at late times.

nature research

Corresponding author(s): *Double-blind peer review submissions: write DBPR and your manuscript number here instead of author names.*

Last updated by author(s): *YYYY-MM-DD*

# Reporting Summary

Nature Research wishes to improve the reproducibility of the work that we publish. This form provides structure for consistency and transparency in reporting. For further information on Nature Research policies, see our Editorial Policies and the Editorial Policy Checklist.

## Statistics

For all statistical analyses, confirm that the following items are present in the figure legend, table legend, main text, or Methods section.

| n/a | Confirmed | |
|---|---|---|
| ☐ | ☒ | The exact sample size (*n*) for each experimental group/condition, given as a discrete number and unit of measurement |
| ☐ | ☒ | A statement on whether measurements were taken from distinct samples or whether the same sample was measured repeatedly |
| ☒ | ☐ | The statistical test(s) used AND whether they are one- or two-sided<br>*Only common tests should be described solely by name; describe more complex techniques in the Methods section.* |
| ☒ | ☐ | A description of all covariates tested |
| ☒ | ☐ | A description of any assumptions or corrections, such as tests of normality and adjustment for multiple comparisons |
| ☒ | ☐ | A full description of the statistical parameters including central tendency (e.g. means) or other basic estimates (e.g. regression coefficient) AND variation (e.g. standard deviation) or associated estimates of uncertainty (e.g. confidence intervals) |
| ☐ | ☒ | For null hypothesis testing, the test statistic (e.g. *F*, *t*, *r*) with confidence intervals, effect sizes, degrees of freedom and *P* value noted<br>*Give P values as exact values whenever suitable.* |
| ☒ | ☐ | For Bayesian analysis, information on the choice of priors and Markov chain Monte Carlo settings |
| ☒ | ☐ | For hierarchical and complex designs, identification of the appropriate level for tests and full reporting of outcomes |
| ☒ | ☐ | Estimates of effect sizes (e.g. Cohen's *d*, Pearson's *r*), indicating how they were calculated |

*Our web collection on statistics for biologists contains articles on many of the points above.*

## Software and code

Policy information about availability of computer code

| | |
|---|---|
| Data collection | We used Nikon-Elements AR to control the fully automated microscopes |
| Data analysis | In-house software has been developed in MATLAB to analyze the collected images (the code is described in the SI) |

For manuscripts utilizing custom algorithms or software that are central to the research but not yet described in published literature, software must be made available to editors and reviewers. We strongly encourage code deposition in a community repository (e.g. GitHub). See the Nature Research guidelines for submitting code & software for further information.

## Data

Policy information about availability of data

All manuscripts must include a data availability statement. This statement should provide the following information, where applicable:

- Accession codes, unique identifiers, or web links for publicly available datasets
- A list of figures that have associated raw data
- A description of any restrictions on data availability

Source data are available for this paper. Additional data that support the plots within this paper and other findings of this study are available at the Zenodo repository (http://doi.org/10.5281/zenodo.3926720).

# Field-specific reporting

Please select the one below that is the best fit for your research. If you are not sure, read the appropriate sections before making your selection.

☐ Life sciences ☐ Behavioural & social sciences ☒ Ecological, evolutionary & environmental sciences

For a reference copy of the document with all sections, see nature.com/documents/nr-reporting-summary-flat.pdf

# Ecological, evolutionary & environmental sciences study design

All studies must disclose on these points even when the disclosure is negative.

| | |
|---|---|
| Study description | We use a microfluidic model system that captures flow disorder and chemical gradients at the pore-scale to quantify the transport and dispersion of the soil-dwelling bacterium Bacillus subtilis in porous media. All experiments include 4 replicates. We observe the spatial distribution of bacteria while displaced by an invading front of a solution of a substance that can trigger bacterial chemotaxis. We observe that chemotaxis strongly modulates the persistence of bacteria in low-flow regions of the pore space. We validate our observations with further investigation of i) chemotaxis in the absence of flow; ii) measurements of local fluid velocity via Particle Image Velocimetry; iii) measurements of the distribution of chemical gradients via a fluorescent tracer; and iv) numerical simulations. |
| Research sample | We use a microfluidics analogue of a porous medium because i) it is transparent, thus enabling direct observations; ii) it is bio-compatible; iii) it can be manufactured at the desired scale (here, with features of size of tens to hundreds of microns). We cultivated B. subtilis because it is a soil-dewlling bacterium, motile, non-pathogen, and exhibits chemotaxis. |
| Sampling strategy | We first inoculate a microfluidics analogue of a porous medium with the prepared bacterial suspension, then we inject a sharp front of a dissolved substance that trigger chemotaxis on the chosen bacterial sample. We collect high-definition images, composed of several individual pictures, every few seconds to observe the bacterial distribution while being displaced by the incoming front. |
| Data collection | We set the microscope (a fully automated Nikon Ti-E) and the camera (Andor Zyla 5.5) to capture one large image every 17 seconds, saving grayscale pictures as png files of 12-bit pixel depth. We performed the experiments with 6X magnification: a large image is composed of 12 pictures (2 rows of 6 pictures each), so that the total field of view is about 10.8 mm x 4.6 mm, corresponding to about 8 x 50 average pore sizes. Grayscale pictures were taken with phase contrast microscopy using a Nikon 4X Plan Fluor Ph1 objective (and the internal scope 1.5X, giving the final 6X magnification) in combination with a phase ring Ph3 (of size larger than the ring present in the selected objective) so that the sample was illuminated almost laterally, thereby obtaining pictures in which the background was dark and bacteria were detected as objects scattering light, appearing bright. |
| Timing and spatial scale | We simultaneously detected the position of individual bacteria as well as the porous landscape of about 8 x 50 = 400 pores of different size and shape where microbes could be transported by the flow or trapped. For each experiment, we took 120 images for a total duration of about 40 min. |
| Data exclusions | No data were excluded. |
| Reproducibility | We repeated each bacteria transport experiment 4 times, as replicates. This is reflected in the figures of the manuscript and the supplementary information. |
| Randomization | Not applicable. We performed each experiment of bacterial transport trying to carefully reproduce the same initial condition for each replicate, to test repeatability. |
| Blinding | Blinding was not relevant to our study. The raw data consisted of high-resolution videos of bacterial transport (4 replicates for each experiment), all conducted prior to the analysis. |

Did the study involve field work? ☐ Yes ☒ No

# Reporting for specific materials, systems and methods

We require information from authors about some types of materials, experimental systems and methods used in many studies. Here, indicate whether each material, system or method listed is relevant to your study. If you are not sure if a list item applies to your research, read the appropriate section before selecting a response.

## Materials & experimental systems

| n/a | Involved in the study |
|---|---|
| ☒ | ☐ Antibodies |
| ☒ | ☐ Eukaryotic cell lines |
| ☒ | ☐ Palaeontology and archaeology |
| ☒ | ☐ Animals and other organisms |
| ☒ | ☐ Human research participants |
| ☒ | ☐ Clinical data |
| ☒ | ☐ Dual use research of concern |

## Methods

| n/a | Involved in the study |
|---|---|
| ☒ | ☐ ChIP-seq |
| ☒ | ☐ Flow cytometry |
| ☒ | ☐ MRI-based neuroimaging |